

See discussions, stats, and author profiles for this publication at: <https://www.researchgate.net/publication/263237648>

Electrocatalytic activity for the oxygen reduction reaction of oxygen-containing nanocarbon synthesized by solution plasma

ARTICLE *in* JOURNAL OF MATERIALS CHEMISTRY · APRIL 2014

Impact Factor: 7.44 · DOI: 10.1039/C4TA01577K

CITATIONS

3

READS

28

4 AUTHORS, INCLUDING:



Takahiro Ishizaki

Shibaura Institute of Technology

82 PUBLICATIONS 861 CITATIONS

SEE PROFILE



Gasidit Panomsuwan

Chulalongkorn University

34 PUBLICATIONS 65 CITATIONS

SEE PROFILE

Cite this: *J. Mater. Chem. A*, 2014, 2, 10589

Electrocatalytic activity for the oxygen reduction reaction of oxygen-containing nanocarbon synthesized by solution plasma†

Takahiro Ishizaki,^{*ab} Satoshi Chiba,^a Youta Kaneko^a and Gasidit Panomsuwan^a

Oxygen-containing nanocarbon materials were successfully synthesized from a mixed solvent of benzene (BZ) and 1,4-dioxane (DO) by solution plasma. TEM observation demonstrated that the synthesized carbons had a diameter in the nanoscale range, their size increased with an increase in the DO content. XRD and Raman spectroscopy measurements revealed that the nanocarbon samples had the (002) characteristic plane of the turbostratic carbon phase and structural defect sites. XPS spectra showed that the nanocarbon sample synthesized from BZ100 consisted of hydroxyl/epoxide groups as the main surface functional groups on the sample surface, whereas the main surface functional groups of the nanocarbon samples synthesized from mixed solvents containing BZ and DO changed from hydroxyl/epoxide groups to carboxyl groups. The O content in the samples increased with an increase in the DO volume ratio in the mixed solvent. The electrocatalytic activity of the synthesized nanocarbon samples for the oxygen reduction reaction (ORR) was investigated electrochemically using cyclic voltammograms (CVs) and linear sweep voltammograms (LSVs) in an O₂-saturated 0.1 M KOH aqueous solution. It was found that the addition of DO to the mixed solvent could only influence the current density, whereas no significant change in the onset potential was observed. The order of the current density of the nanocarbon samples for the ORR was as follows: BZ90 + DO10 > BZ100 > BZ70 + DO30 > BZ50 + DO50. The number of electron transfers for the ORR of the nanocarbon samples estimated by Koutechy–Levich (K–L) plots was about three at low potentials, indicating the coexistence of two- and four-electron reduction of O₂. The oxygen-containing functional groups formed on the carbon surface and structural defects seemed to play the key roles in enhancing the electrocatalytic activity for the ORR rather than the total oxygen content in the nanocarbon samples.

Received 1st April 2014
Accepted 22nd April 2014

DOI: 10.1039/c4ta01577k

www.rsc.org/MaterialsA

1. Introduction

The demand for energy storage and conversion devices such as fuel cells, electrochemical capacitors, and metal–air batteries is growing year by year. To satisfy this demand, it is vital to highly functionalize these devices.¹ The development of electrode materials that provide high energy, high power, and a long life cycle is a key factor for realizing state-of-the-art lithium-ion batteries,^{2,3} fuel cells,^{4,5} and electrochemical capacitors.^{6–8} Oxygen reduction reaction (ORR) is a critical process in energy conversion devices. The ORR is normally catalyzed on a cathode by Pt-based catalysts. To improve the reaction efficiency, high Pt loading amounts are required. However, Pt consumption must be reduced because of the limited natural resources and high cost of Pt. In addition, the instability and deactivation by CO

poisoning and methanol crossover effect of Pt-based catalysts have also hindered the large-scale application of energy conversion devices.⁹ Thus, there have been many attempts to develop Pt-free catalysts.^{10–13}

Nanocarbons with sp² bonds having abundant free-flowing π electrons such as carbon nanotubes and graphene have attracted much attention as promising next-generation energy conversion materials because of their superior advantages, such as high electronic conductivity, mechanical and chemical stability, and high specific surface area. Many attempts have been made to improve the nanocarbon properties by controlling their structures and electron states. The doping of nitrogen in nanocarbon materials would be an effective method for improving the performance of the energy storage and conversion devices because nitrogen chemically binds to the carbon lattice of the nanocarbon materials. Moreover, nitrogen has a comparable atomic size and higher electronegativity as compared to carbon.^{14–17} Owing to the presence of electron-rich nitrogen, the π electrons of the nanocarbon materials can be activated by conjugating them with the lone-pair electrons from nitrogen dopants. Recently, Yang *et al.* reported that nanocarbon materials can be activated by doping with electron-

^aDepartment of Material Science and Engineering, Faculty of Engineering, Shibaura Institute of Technology, 3-7-5 Toyosu, Koto-ku, Tokyo 135-8548, Japan. E-mail: ishizaki@shibaura-it.ac.jp; Fax: +81-3-5859-8115; Tel: +81-3-5859-8115

^bJST-CREST, 4-1-8 Honcho, Kawaguchi, Saitama 332-0012, Japan

† Electronic supplementary information (ESI) available. See DOI: 10.1039/c4ta01577k

deficient boron.¹⁸ These results indicate that breaking the electroneutrality of sp^2 carbon to create charged sites favourable for O_2 adsorption would be an effective strategy for creating a novel metal-free catalyst for the ORR.

There is a possibility that the doping of oxygen could break the electroneutrality of sp^2 carbon because the dopant is electron-rich, thus leading to the activation of carbon π electrons for effective utilization by O_2 . In addition, the electronegativity of oxygen is larger than that of nitrogen ($\chi_C = 2.55$, $\chi_O = 3.44$, and $\chi_N = 3.04$). Suggs *et al.* reported that using first-principles density-functional theory (DFT) calculations, oxygen doping was shown to modify the π conjugation of carbon nanotubes and impact the near-infrared band gaps.¹⁹ On the other hand, it has been reported that the introduction of surface functional groups such as oxygen on carbon materials is a promising strategy to increase the energy density of electrodes.^{2,20–23} However, to our knowledge, there has been no report on the electrocatalytic activity for the ORR of oxygen-containing carbon materials.

Cold plasma in a liquid phase, so-called solution plasma, has attracted considerable attention in the field of materials science and for applications, such as nanoparticle synthesis, surface modification, and decomposition of organic dyes^{24–28} because the solution plasma can realize a high reaction rate at low temperature and atmospheric pressure. Moreover, the solution plasma holds the promise of paving the way for molecular assembling technology because it can generate highly reactive radicals on the terminals of the molecular framework. Kang *et al.* reported that through a solution plasma process using benzene as a raw material, nanocrystalline graphite (NCG) was successfully synthesized under specific conditions.²⁹ In a plasma process in a liquid phase, two routes for the synthesis of carbon nanomaterials have been reported. One is the sputtering of graphite electrodes in a liquid medium (*e.g.*, ethanol, water, liquid nitrogen).^{30,31} In this case, high energy would be required to sputter the graphite electrode. Thus, it is difficult to precisely control the chemical reaction due to the high energy input. The other route is the decomposition of an organic liquid by plasma. In this process, by controlling the plasma conditions such as applied voltage, frequency, and pulse width, one can generate cold plasma to control the chemical reaction in the liquid phase. Many attempts have been made by using aromatic liquid precursors such as benzene, toluene, and xylene for the synthesis of carbon materials.^{29,32,33} Therefore, by selection of suitable precursors, the hetero-atoms containing nanocarbon would be expected to be synthesized by solution plasma.

In this paper, we report the synthesis of oxygen-containing nanocarbon materials from mixed aromatic liquid precursors by solution plasma at room temperature for the first time. The correlation between the physicochemical properties and the electrocatalytic activity for the ORR activity was investigated and discussed in considerable detail.

2. Experimental procedures

Benzene ($\geq 99.5\%$ purity) was purchased from Wako Pure Chemical Industries. 1,4-Dioxane ($\geq 99.5\%$ purity), ethanol ($\geq 99.5\%$ purity), acetone ($\geq 99.5\%$ purity), and 0.1 M potassium

hydroxide aqueous solution were purchased from Kanto Chemical Co. Inc. Nafion solution (5%) and 20 wt% Pt/Vulcan XR-72C were purchased from Sigma-Aldrich. Ultrapure water (18.2 M Ω cm) was obtained from a RFD250NB Aquarius water purification system. All chemicals were used without further purification.

Benzene (BZ) and 1,4-dioxane (DO) were used as raw materials. The BZ and DO were mixed at volume ratios of 10 : 0, 9 : 1, 7 : 3, and 5 : 5. The nanocarbon materials synthesized from the mixed solutions of BZ and DO at these volume ratios are hereafter denoted as BZ100, BZ90 + DO10, BZ70 + DO30, and BZ50 + DO50, respectively. 100 mL of the mixed solvents were used as reaction fields of the solution plasma process. The experimental setup of the solution plasma process was the same as that used in our previous studies.³⁴ This system consists of a pair of 1.0 mm-diameter tungsten wire as the electrode (99.95% purity, Nilaco Corporation) placed at the center of a glass vessel, and the plasma was driven by a bipolar DC pulse power supply (MPP-HV04, Kurita Seisakusho Co., Ltd., Kyoto, Japan). The electrode gap between the two tungsten wires was set at 0.5 mm. The applied voltage was varied from 1.2 to 1.6 kV depending on the mixing ratio. The pulse frequency and pulse width were employed at 20 kHz and 1 μ s, respectively. The discharge time was kept constant to be 10 min for all experiments. After the discharge, the synthesized black soots were separated from the solution by filtration, followed by washing with ethanol several times in order to remove the soluble organic contaminants.

The morphologies of the synthesized nanocarbon samples were observed by scanning electron microscopy (SEM; JEOL-JSM6010LA) at an accelerating voltage of 10 kV. Transmission electron microscopy (TEM) and high-resolution transmission electron microscopy were carried out with a JEOL, JEM-2100 with an acceleration voltage of 200 kV. The specific surface area (SSA) was measured using a Micrometrics Gemini 2360 instrument equipped with VacPrep 061. The samples were annealed under vacuum at 300 °C for 3 h before measurement. X-ray diffraction (XRD) patterns were acquired using a Rigaku Ultima IV X-Ray diffractometer with Cu K α radiation (40 kV, 40 mA) at a scanning rate of 4° min^{−1}. The Raman scattering spectra were recorded on a JASCO NSR-5100 system with an excitation wavelength of 532.1 nm. The chemical bonding states of the synthesized nanocarbon samples were analyzed by X-ray photoelectron spectroscopy (XPS; JEOL-JPS9010MC) using Mg K α radiation ($h\nu = 1253.6$ eV) operating at 12 mA and 25 kV. All spectra were calibrated by setting the C 1s photoemission peak for sp^2 -hybridized carbons to 284.5 eV and deconvoluted by mixed Gaussian–Lorentzian product functions. The atomic composition of the synthesized samples was estimated using XPS.

A rotating glassy carbon (GC) and nanocarbon-modified GC disk electrodes with diameters of 3.0 mm were used as the working electrodes in this study. Prior to modification, the GC electrode was polished with 1.0 μ m diamond paste and 0.05 μ m alumina paste. It was then ultrasonically cleaned in ultrapure water for 10 min. 10 mg of nanocarbon, 480 μ L of ethanol, 480 μ L of ultrapure water, and 40 μ L of 5 wt% Nafion® aqueous solution were mixed and ultrasonically dispersed at least 30 min

for the preparation of the nanocarbon catalytic ink. After that, 3 μL of well-dispersed catalytic ink was pipetted onto the polished GC electrode and allowed to dry in air for 6 h. Cyclic voltammograms (CVs), linear sweep voltammograms (LSVs), and current-time (i - t) chronoamperometric responses were recorded on a computer-controlled ALS-CH instrument electrochemical analyzer model 704ES (BAS, Co.) in a three-electrode system with 0.1 M KOH as the electrolyte. A Pt wire and an Ag/AgCl (KCl sat.) electrode were used as the counter and reference electrodes, respectively. Before all the measurements, N_2 gas was introduced into the electrolyte for 20 min to remove the dissolved O_2 gas. After that, O_2 gas was introduced into the electrolyte for 20 min to estimate the electrocatalytic activity of the ORR. The O_2 gas was passed on the solution level in the electrochemical cell during the measurements. All the experiments were performed at room temperature.

3. Results and discussion

The SEM images of the synthesized carbons are illustrated in Fig. 1(a)–(d). It can be seen that the nanocarbon samples are composed of uniform nanosized particles. Upon increasing the DO content, the carbon particles tend to be formed as larger agglomeration. A more detailed morphology of nanocarbons was investigated by TEM, as displayed in Fig. 2(a)–(d). Most of the particles have a ball-like shape, whereas other shapes, such as carbon nanotubes or carbon flakes or fibers, cannot be observed. The carbon particles are agglomerated with each other by coalescence of the surface forming chains. Another obvious investigation is a slight increase in particle size when the DO content increases. The diameter of carbon particles is in the range of 20 to 50 nm. The HRTEM image and the corresponding selected area electron diffraction (SAED) pattern are shown in Fig. 3(a) and (b), respectively. The graphite-like layered structure is clearly observed from the HRTEM image, indicating good crystallinity of synthesized nanocarbon. The SAED corresponding to the area in Fig. 3(a) shows well-defined ring patterns, which are associated with (002), (100), and (110) planes of nanocarbons. More discussion on structural properties will be shown later in XRD and Raman analyses. To gain deeper insight into the morphological feature of the synthesized carbons, the specific surface area was evaluated using the Brunauer–Emmett–Teller (BET) method based on the adsorption data in the relative pressure (P/P_0) range of 0.05–0.30 (Fig. S1†). The calculated BET surface areas of all nanocarbon samples are shown in Table 1. It is found that the nanocarbon synthesized from BZ100 possesses the specific surface area of $176 \text{ m}^2 \text{ g}^{-1}$. A further increase in the DO content leads to a progressive enhancement in the surface area up to $225 \text{ m}^2 \text{ g}^{-1}$.

Fig. 4(a) shows XRD patterns of the nanocarbon samples synthesized from BZ100, BZ90 + DO10, BZ70 + DO30, and BZ50 + DO50. All samples show the same XRD pattern with a broad peak at $\sim 24^\circ$, corresponding to the (002) characteristic plane of the turbostratic carbon phase.²⁸ The full-width at half-maximum (FWHM) values of the (002) peak are gradually broadened with an increase in the DO content, indicating a decrease in the crystallite size of the samples. The calculated

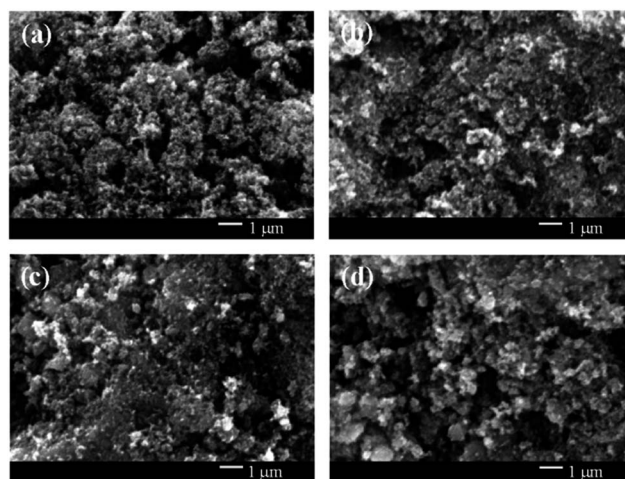


Fig. 1 SEM images of the nanocarbon samples synthesized from (a) BZ100, (b) BZ90 + DO10, (c) BZ70 + DO30, and (d) BZ50 + DO50.

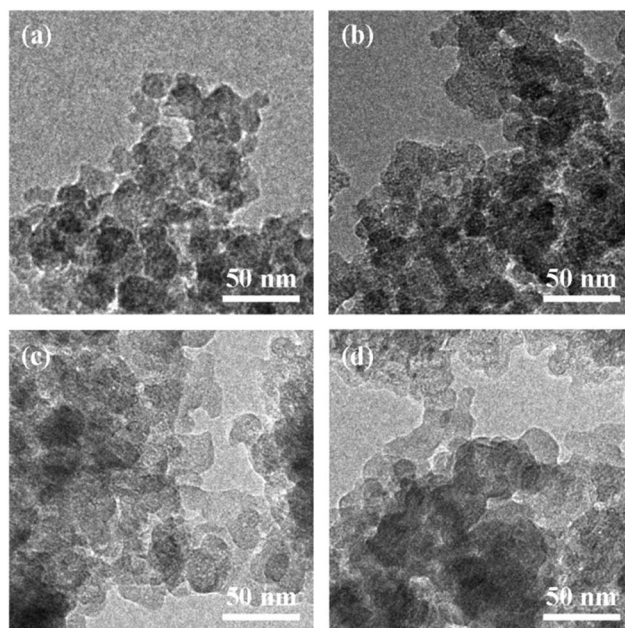


Fig. 2 BF-TEM images of the nanocarbon samples synthesized from (a) BZ100, (b) BZ90 + DO10, (c) BZ70 + DO30, and (d) BZ50 + DO50.

interlayer spacing of the nanocarbon samples synthesized from BZ100, BZ90 + DO10, BZ70 + DO30, and BZ50 + DO50 are estimated to be 0.3587, 0.3846, 0.4207, and 0.4318 nm, respectively. These calculated values are greater than that of ideal graphite (0.3348–0.3360 nm).^{35,36} Further structural information was estimated using Raman spectroscopy. Raman analysis is a useful tool for providing detailed information about the structure of graphitic materials. Fig. 4(b) shows the Raman spectra of the nanocarbon samples synthesized from BZ100, BZ90 + DO10, BZ70 + DO30, and BZ50 + DO50. There are two typical bands in all the spectra. The first band corresponding to the D band at approximately 1350 cm^{-1} is related to a disordered structure. The presence of the D band peak is a typical characteristic of

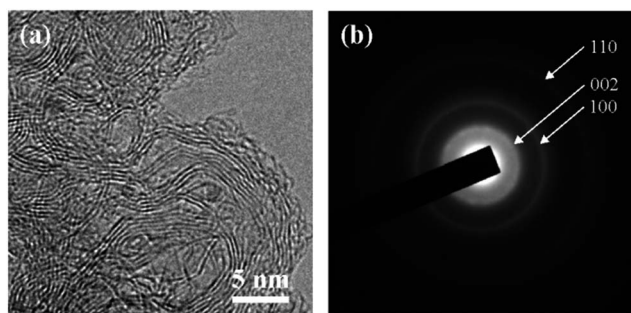


Fig. 3 (a) HRTEM and (b) the corresponding SAED pattern of nanocarbon samples synthesized from BZ100.

Table 1 Specific surface area (S_{BET}), mean particle size deduced from TEM image, and structural properties obtained from XRD and Raman spectroscopy analyses

Raw material	S_{BET} ($\text{m}^2 \text{g}^{-1}$)	Structural properties		
		d_{002} (nm)	$I_{\text{D}}/I_{\text{G}}$	L_{a} (nm)
BZ100	176.3	0.3587	0.93	20.6
BZ90 + DO10	190.8	0.3846	0.94	20.4
BZ70 + DO30	222.1	0.4207	0.98	19.7
BZ50 + DO50	225.8	0.4318	0.88	21.7

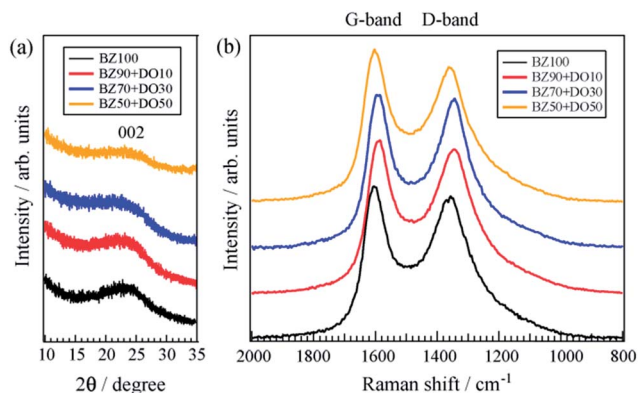


Fig. 4 (a) XRD patterns and (b) Raman spectra of the nanocarbon samples synthesized from BZ100, BZ90 + DO10, BZ70 + DO30, and BZ50 + DO50.

chemically synthesized carbon nanomaterials.^{37–39} The second band corresponding to the G band at approximately 1590–1600 cm^{-1} is attributed to the first-order scattering of the stretching vibration mode E_{2g} observed for the sp^2 carbon domain. The degree of disorder for the synthesized nanocarbon materials is estimated quantitatively using the ratio of intensities of the D and G bands, *i.e.*, $I_{\text{D}}/I_{\text{G}}$.^{38,39} The $I_{\text{D}}/I_{\text{G}}$ values can be used as an indicator of the number of defect sites for the synthesized nanocarbon materials. The $I_{\text{D}}/I_{\text{G}}$ values of the nanocarbon samples synthesized from BZ100, BZ90 + DO10, BZ70 + DO30, and BZ50 + DO50 were found to be 0.93, 0.94, 0.98, and 0.88, respectively. It has been reported that with an

increase in the $I_{\text{D}}/I_{\text{G}}$ values, the number of defect sites of the carbon samples increases. Thus, the nanocarbon materials synthesized from BZ70 + DO30 has the highest number of defect sites among all the samples synthesized in this study. Except for the nanocarbon materials obtained from BZ50 + DO50, the $I_{\text{D}}/I_{\text{G}}$ values increases with an increase in the DO content. Furthermore, the $I_{\text{D}}/I_{\text{G}}$ value is also related to the in-plane crystallite size L_{a} , which can be determined using the Tuinstra-Koenig relationship as follows:⁴⁰

$$L_{\text{a}} = C\lambda^4(I_{\text{D}}/I_{\text{G}})^{-1} \quad (1)$$

where C is a constant ($2.4 \times 10^{-10} \text{ nm}^{-3}$) and λ is the Raman excitation wavelength (532.1 nm). The values of L_{a} are consistent with the interdefect distance on the surface of the graphene sheet,⁴¹ which are listed in Table 1. By combining the data from XRD and Raman spectroscopy, it suggests that the increase of the oxygen content in the nanocarbon materials can induce more defect sites due to the high reactivity of the oxygen molecules. The change in interlayer spacing and FWHM is strongly related to the structural defects in the carbon structure. However, the $I_{\text{D}}/I_{\text{G}}$ value decreases when the DO content in the mixed solvent reaches 50 vol%. This may be attributed to structural differences among the nanocarbon samples, *i.e.*, the configuration of bonds and/or the nature of the oxygen-containing nanocarbon. It has been known that various oxide groups with sp^3 bond (*e.g.*, $-\text{COOH}$, $=\text{CO}$, $-\text{OH}$) likely formed at the defect sites and nanoholes.⁴² This may be a possible cause for the expansion of interlayer spacing and lattice relaxation. The evolution of oxide groups and bonding configuration will be shown and discussed by XPS measurement.

In order to probe the chemical bonding states of the synthesized nanocarbon samples, XPS measurements were performed. Fig. 5 shows the high-resolution XPS C 1s and O 1s spectra of the samples synthesized from BZ100, BZ90 + DO10, BZ70 + DO30, and BZ50 + DO50. The XPS spectra reveal that the O/C atomic ratio increases from 0.044 to 0.227 with an increase in the DO content in the mixed solution. The C 1s spectrum of the nanocarbon synthesized from BZ100 [Fig. 5(a)] is deconvoluted into three peaks corresponding to the sp^2 -hybridized carbons (peak 1 at 284.5 eV), the sp^3 -hybridized carbons (peak 2 at 285.3 eV), and carbon atoms singly bonded to oxygen (peak 3 at 286.5 eV).^{43,44} On the other hand, as shown in Fig. 5(b–d), the C 1s spectra reveal that the nanocarbon samples synthesized from the mixed solutions of BZ and DO have two additional peaks corresponding to carbon atoms doubly bonded to oxygen (peak 4 at 287.5–288.0 eV) and a weak peak (peak 5, just below 292.0 eV) resulting from a $\pi \rightarrow \pi^*$ shake-up process in addition to the above-mentioned three peaks. The O 1s spectra of the carbon samples synthesized are deconvoluted into four peaks corresponding to carbonyl (peak 1 at 531.6 eV), hydroxyl/epoxide (peak 2 at 532.5 eV), ester (peak 3 at 533.4 eV), and carboxylic (peak 4 at 534.4 eV) groups. The relative component contents determined from each sub-peak area of C 1s and O 1s spectra for all samples are summarized in Table 2. From the XPS spectra, the carboxyl groups can be introduced on the sample surfaces. With an increase in the number of carboxyl groups on

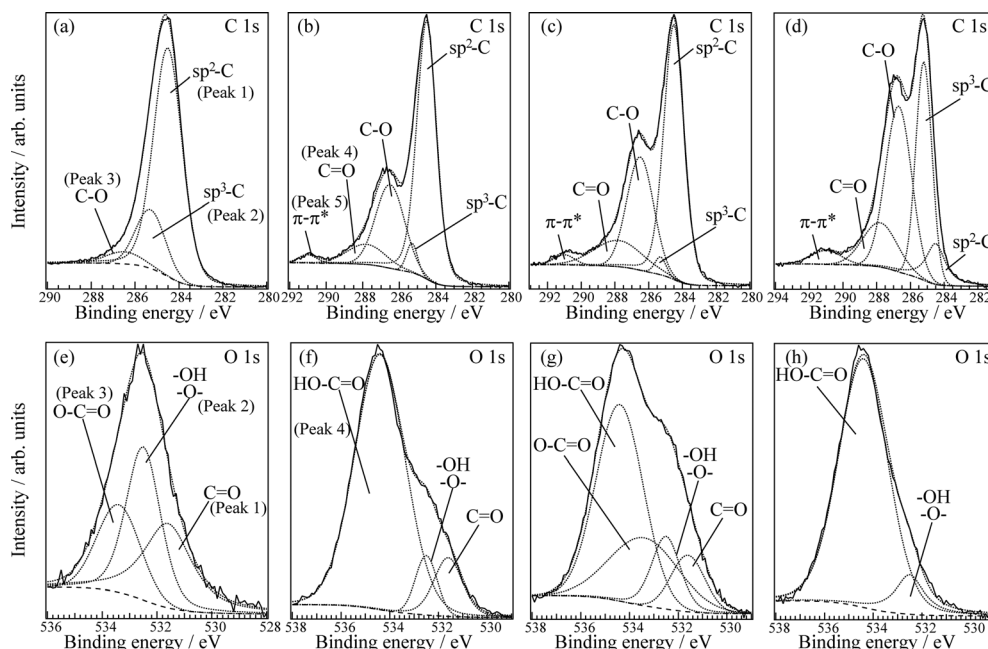


Fig. 5 XPS C 1s spectra of the nanocarbon samples synthesized from (a) BZ100, (b) BZ90 + DO10, (c) BZ70 + DO30, and (d) BZ50 + DO50. XPS O 1s spectra of the samples synthesized from (e) BZ100, (f) BZ90 + DO10, (g) BZ70 + DO30, and (h) BZ50 + DO50.

the sample surface, the number of carbonyl groups on the sample surface decreases. These results indicate that due to the presence of the DO solvent in the raw materials, the main surface functional groups introduced on the carbon samples change from hydroxyl/epoxide groups to carboxylic groups. A schematic illustration of the proposed structural model for the nanocarbon structures synthesized by solution plasma as a function of the DO content in the raw materials is depicted in Fig. 6.

To investigate the electrocatalytic activity for the ORR of the nanocarbon samples, cyclic voltammetry was performed in an O₂-saturated 0.1 M KOH aqueous solution within the potentials ranging from 0.2 to −1.0 V at a scanning rate of 50 mV s^{−1}. Fig. 7 shows the cyclic voltammograms (CVs) obtained from the electrodes modified by the nanocarbon samples synthesized from BZ100, BZ90 + DO10, BZ70 + DO30, and BZ50 + DO50. An obvious reduction peak can be observed from the CVs for all

nanocarbon samples. After subtracting the current-density baseline (measured in N₂-saturated 0.1 KOH solution), the nanocarbon sample synthesized from BZ90 + DO10 has the current density of 0.84 mA cm^{−2}, which is the highest value when compared to other samples (Fig. S12†). However, the occurrence of the reduction peak remains unchanged at the same potential of about −0.30 V. The relationship between the values of the reduction peak current after subtraction of the baseline and the atomic O/C ratio is shown in Fig. 8. The reduction peak current is found to be independent of the atomic O/C ratio in the synthesized nanocarbon samples. This result indicates that the electrocatalytic activity of the nanocarbon samples for the ORR relates to the other factors, such as structural defects and surface functional groups. A comparison of linear sweep voltammograms (LSVs) obtained from different electrodes at a rotation rate of 2000 rpm is shown in Fig. 9(a). On the GC electrode, two-reduction steps, both attributed to the

Table 2 Detailed deconvolution of XPS C 1s and O 1s spectra of the nanocarbons synthesized from BZ100, BZ90 + DO10, BZ70 + DO30, and BZ50 + DO50

XPS	Peak	Bonding	Peak position (eV)	Raw material			
				BZ100	BZ90 + DO10	BZ70 + DO30	BZ50 + DO50
C 1s	1	sp ² -C	284.5	76.6%	60.8%	54.4%	10.0%
	2	sp ³ -C	285.3	18.7%	3.5%	2.0%	32.4%
	3	C-O	286.5	4.7%	25.9%	29.2%	39.6%
	4	C=O	287.8	—	8.3%	12.4%	14.1%
	5	π-π*	291.0	—	1.5%	2.0%	3.9%
O 1s	1	C=O	531.6	39.5%	7.7%	12.7%	11.1%
	2	-O-, -OH	532.5	35.6%	11.3%	10.5%	—
	3	O-C=O	533.4	24.9%	—	25.7%	—
	4	HO-C-O	534.4	—	81%	51.1%	89.9%

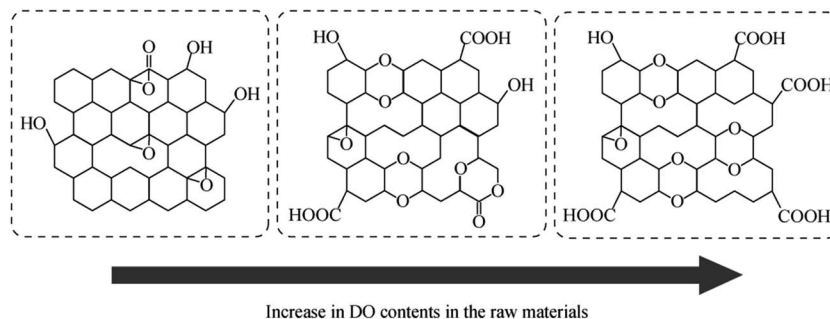


Fig. 6 Schematic illustration of the proposed nanocarbon structures as a function of the DO content in the raw materials.

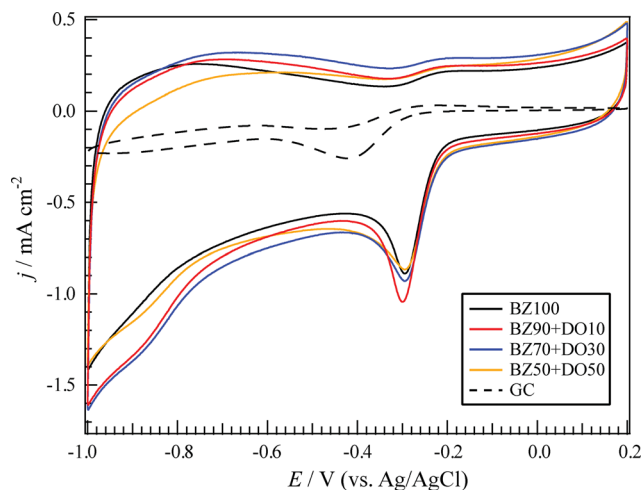


Fig. 7 CVs of the nanocarbon samples synthesized from BZ100, BZ90 + DO10, BZ70 + DO30, and BZ50 + DO50 in O_2 -saturated 0.1 M KOH solution with a scan rate of 50 mV s^{-1} .

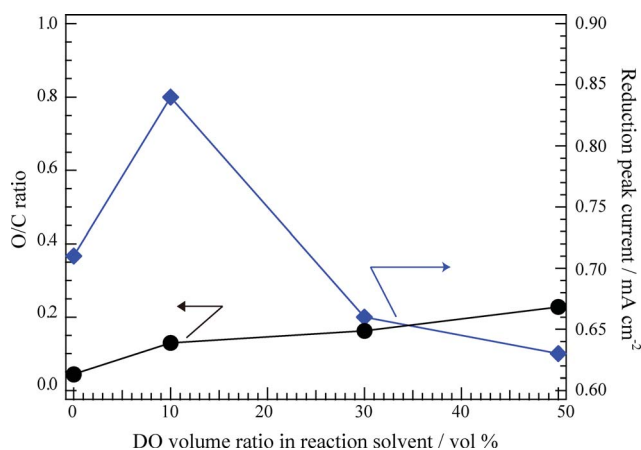


Fig. 8 Relationship between the ORR peak current after subtraction of the baseline and the atomic O/C ratio as a function of the DO volume ratio (vol%) in the raw materials.

two-electron reduction of O_2 to HO_2^- , are observed. In first reduction step, the process at around -0.45 V is mediated by native active quinone-like groups with superoxide anions as the

intermediate. The second reduction step is a direct two-electron reduction on the GC electrode surface.⁴⁵ In contrast, the modification of the nanocarbon samples on the GC electrode surface shows a relatively larger current density when compared to the bare GC electrode. To gain further insight into the ORR mechanism of the nanocarbons, LSVs at different rotation speeds (250–3000 rpm) were performed for the four nanocarbon sample-modified electrodes in an O_2 -saturated 0.1 M KOH aqueous solution within the potentials ranging from 0.0 to -1.0 V under a scanning rate of 10 mV s^{-1} . The limiting current densities of all samples increase with an increase in the rotation speed (Fig. SI3†). From the LSV measurement, the electron transfer number can be calculated using the Koutechy–Levich (K–L) equation:⁴⁶

$$\frac{1}{j} = \frac{1}{j_k} + \frac{1}{j_d} = -\frac{1}{nFkC_O^b} - \frac{1}{0.62nFD_O^{2/3}\nu^{-1/6}C_O^b\omega^{1/2}} \quad (2)$$

where j is the measured current density, j_k and j_d are the kinetic and diffusion-limited current densities, respectively, n is the number of electrons transferred per O_2 molecule, k is the rate constant for O_2 reduction, F is the Faraday constant (96485 C mol^{-1}), D_O is the diffusion coefficient of oxygen ($1.9 \times 10^{-5} \text{ cm}^2 \text{ s}^{-1}$),⁴⁷ ν is the kinematic viscosity of the solution ($0.01 \text{ cm}^2 \text{ s}^{-1}$),⁴⁸ C_O^b is the concentration of oxygen in the bulk ($1.2 \times 10^{-6} \text{ mol cm}^{-3}$),⁴⁹ and ω the rotation speed. Fig. 9(b) shows the K–L plots obtained from the LSV data of the carbon synthesized from BZ90 + DO10 at the potentials from -0.4 to -0.8 V . The K–L plot of the GC electrode and the other nanocarbon sample-modified electrodes are presented in Fig. SI4.† The slopes of the K–L lines at the potentials between -0.4 and -0.7 V are almost parallel and become lower at the potential above -0.8 V . This indicates that there are two reduction pathways in the ORR activity. Moreover, the intercept of the extrapolated K–L lines are not close to zero, which proves that the O_2 reduction is almost under mixed kinetic-diffusion control. By knowing the slope of the K–L line, the n value for all nanocarbon samples at different potentials can be calculated from eqn (2). Fig. 9(d) shows the comparison of calculated n values for all nanocarbon samples at the potential from -0.4 to -0.9 V . The n values of the bare GC electrode are close to two at low potentials ($E > -0.6 \text{ V}$), indicating that the reduction of oxygen produces peroxide. For the nanocarbon-modified electrodes, the n values are close to three at low potentials, indicating the coexistence of two- and

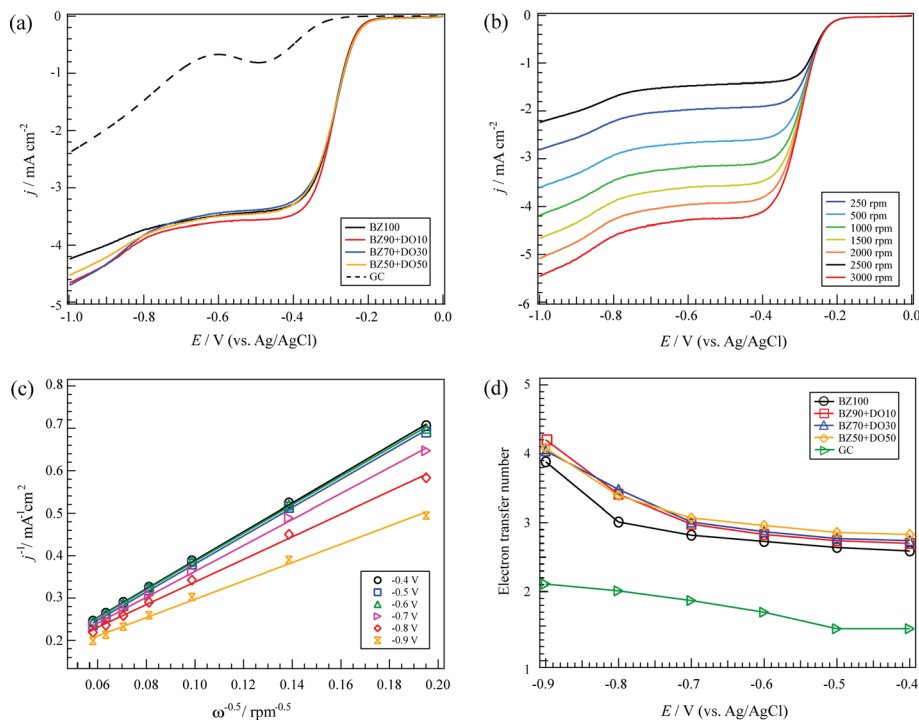


Fig. 9 (a) Comparison of LSVs for ORR obtained at different electrodes (GC, the nanocarbon samples synthesized from BZ100, BZ90 + DO10, BZ70 + DO30, and BZ50 + DO50) with a rotation rate of 2000 rpm and a scanning rate of 10 mV s^{-1} . (b) LSVs of the nanocarbon sample synthesized from BZ90 + DO10 at different rotation speeds. (c) Corresponding K–L plots of the nanocarbon samples synthesized from BZ90 + DO10 at the potentials between -0.4 and -0.9 V . (d) Calculated n values of different electrodes (GC, the nanocarbon samples synthesized from BZ100, BZ90 + DO10, BZ70 + DO30, and BZ50 + DO50) at the potentials between -0.4 and -0.9 V .

four-electron reduction of O_2 . At more negative potentials, the n values of the nanocarbons synthesized from the BZ90 + DO10-, BZ70 + DO30-, and BZ50 + DO50-modified electrodes gradually increase close to four, indicating that the hydrogen peroxide is further reduced to water in this range of potentials. An increase in overpotential provides more activation energy to favour the four-electron ORR, and an increase in n values with a negative shift in potential is observed. This may suggest that the presence of DO in the raw materials can contribute to the improvement of the ORR activity. The reason may also be attributed to the high electronegativity of oxygen, which can help to create dipoles on the nanocarbon surfaces. However, the ORR activity performance of these nanocarbon samples is still not as good as that of commercial Pt/carbon in terms of the reduction potential of O_2 and the current density.

As mentioned above, the electrocatalytic activity of the nanocarbon samples for the ORR is not proportional to the total oxygen content, which first increases and then decreases with an increase in the oxygen content. The electrocatalytic activity is directly linked to its textural properties because the higher surface area should facilitate the oxygen transfer in the catalyst. Although the specific surface area is found to enhance with the increase of the total oxygen content (Table 1), the electrocatalytic activity for the ORR does not proportionally increase with the surface area. Therefore, the electrocatalytic activity of the nanocarbon sample may be dominated by other factors rather than the total oxygen content and surface area. From the

physical and chemical data, the structural defects and surface functional groups seem to play a significant role in influencing electrocatalytic activity. Let us first consider the structural defects, the nanocarbon sample synthesized from BZ90 + DO10 has slightly higher defect sites than the nanocarbon samples synthesized from BZ100 and BZ50 + DO50. These defect sites may result in charge localization and the coupled chemisorptions of oxygen. Moreover, the oxygen atoms may induce more strain and structural deformation in the carbon framework, which would enhance the ORR activity. From the XPS analysis, the incorporation of oxygen into nanocarbon materials induces the oxygen-containing functional groups on the nanocarbon surface and polarizes the adjacent carbon atoms to enhance the adsorption of O_2 , thus readily attracting electrons for facilitating the ORR. It has been reported that the oxygen-containing groups can impart active sites for the ORR and provide additional electrons to the aromatic π system of the nanocarbon, which thus effectively improves the electrocatalytic activity for the ORR.^{50,51} Furthermore, the difference in the surface functional groups can also induce the reactivity of the neighbouring bonded carbon atoms by changing the electronic structures, and so the nanocarbon sample synthesized from BZ90 + DO10 has faster reaction kinetics with a greater number of transferred electrons per oxygen molecule. The order of the surface functional groups affecting the ORR activity is as follows: carboxyl > carbonyl > hydroxyl groups.

It has been reported that there are two typical adsorption modes for an oxygen molecule, the side-on mode (known as the Yeager model), and the end-on mode (known as the Pauling model), as shown in Fig. 10.^{52–54} The oxygen molecule adsorbed on the active sites of the carbon by the side-on mode tends to get four electrons to release OH^- by breaking the O–O bond of the O_2 molecules, thus catalyzing the ORR in a four-electron pathway to produce OH^- .⁵⁵ On the other hand, the oxygen molecule adsorbed on the active sites of the carbon by the end-on mode is beneficial for catalyzing the ORR in a two-electron pathway to produce HO_2^- .^{55,56} The n values of our synthesized nanocarbon samples are close to three at low potentials. Thus, the oxygen molecule can be adsorbed slightly by the side-on mode on the nanocarbon samples synthesized from the raw materials containing DO and the ORR on these nanocarbon samples can proceed *via* the two-electron pathway. The carbon atom in the carbonyl group is relatively strongly electropositive, which is beneficial for adsorbing an oxygen atom of the oxygen molecule, so the nanocarbon samples synthesized from the raw materials containing DO exhibit higher ORR activity as compared to those synthesized from the raw materials without DO. Although the electropositivity of the carbon atom in the carboxyl group is stronger than that in the carbonyl group, the ORR activity of the nanocarbon samples from the raw materials containing DO is higher than that of the samples from the raw

materials without DO. It is possible that the oxygen anion in the carboxyl group can weaken the bonds between the carbon and oxygen and exhibit the highest ORR activity. All the oxygen-containing groups can be easily bonded to H_2O_2 , and thus, it is favourable for further reduction of H_2O_2 to H_2O , so the n values of the nanocarbon samples from the raw materials containing DO are higher than those from the nanocarbon samples without DO at the potentials ranging from -0.4 to -0.9 V.

To further investigate the stability of all nanocarbons, the i - t chronoamperometric response was observed. For comparison, commercial Pt/carbon was also tested, as shown in Fig. 11(a). The samples were held at -0.5 V with a rotation speed of 1500 rpm for 45 000 s in an O_2 -saturated 0.1 M KOH solution. After operating for 45 000 s, the current of Pt/carbon becomes remarkably decreased to 67%, on the other hand, all the nanocarbons are more stable with a much slower attenuation rate than commercial Pt/carbon. This result is evidence that the nanocarbons synthesized from solution plasma have much better stability in the electrooxidation reaction in alkaline media than the commercial Pt/carbon. The stability of nanocarbons is in the order BZ90 + DO10 (95%), BZ50 + DO50 (93%), BZ100 (93%), and BZ70 + DO30 (90%). The most active nanocarbon (BZ90 + DO10) also has the best stability. The poorest stability of BZ70 + DO30 seems to be attributed to the highest defect density in the structure as indicated by Raman Spectroscopy. Furthermore, the tolerance to the methanol crossover effect of nanocarbons was evaluated by the i - t chronoamperometric response, as shown in Fig. 11(b). A sharp decrease in current upon the addition of 1 mL methanol at 1200 s for the commercial Pt/carbon can be observed. However, the current of all nanocarbons remains nearly unchanged after the addition of methanol, indicating the high selectivity toward the ORR and good tolerance to the methanol crossover effect. The comparative CV curves of all nanocarbons and commercial Pt/carbon before and after adding methanol are demonstrated in Fig. S15.† All synthesized carbons do not show any response, whereas the disappearance of the ORR peak is observed for commercial Pt/carbon.

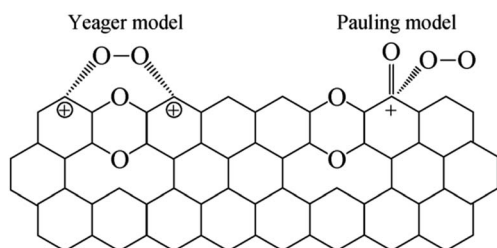


Fig. 10 Oxygen adsorption models for ORR.

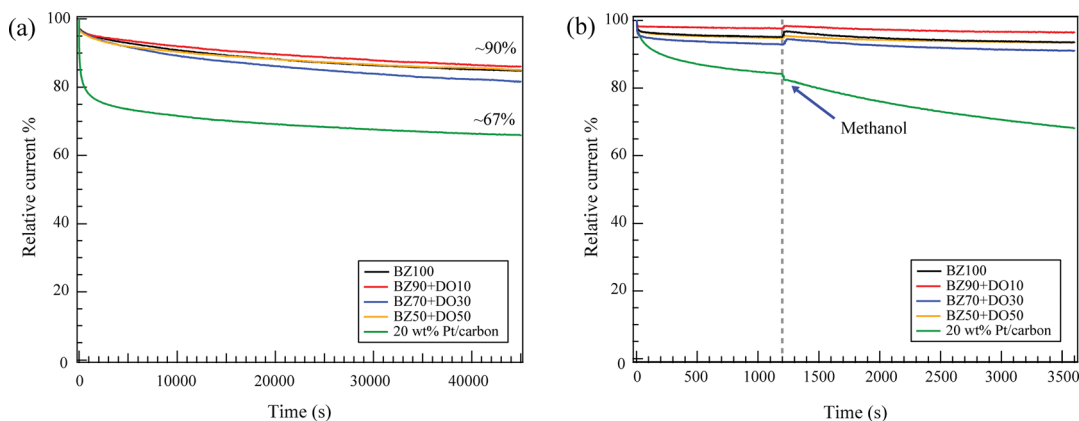


Fig. 11 (a) i - t chronoamperometric responses of the nanocarbon samples synthesized from BZ100, BZ90 + DO10, BZ70 + DO30, BZ50 + DO50, and commercial 20 wt% Pt/carbon in an O_2 -saturated 0.1 M KOH solution with a rotation speed of 1500 rpm at a potential of -0.5 V and (b) i - t chronoamperometric responses for all nanocarbon samples and commercial 20 wt% Pt/carbon with 1 mL methanol added at around 1200 s.

4. Conclusions

Oxygen-containing nanocarbon materials were successfully synthesized by a solution plasma process for the first time. TEM observation showed that the size of synthesized carbon samples was at the nanometer scale ranging from 20 to 50 nm with the graphite-like layered structure. From XRD and Raman spectroscopy measurements, the nanocarbon samples exhibited the turbostratic carbon phase, and the defect site tended to increase with increasing DO content in raw materials. The XPS measurement revealed that the nanocarbon sample synthesized from BZ100 had hydroxyl/epoxide groups as the main surface functional groups on the sample surface, whereas the main surface functional groups of the nanocarbon samples synthesized from mixed solvents containing BZ and DO changed to carbonyl and carboxyl groups.

For the electrocatalytic activity of the synthesized nanocarbon samples, the ORR peak could be clearly observed at the potentials of about -0.3 V for all samples. Upon changing the DO content in the raw material, the onset potential for the ORR remained unchanged, while the highest peak current was found for the nanocarbon synthesized from BZ90 + DO10. The electrocatalytic activity for the ORR seemed to be associated with the surface functional groups rather than with the total oxygen content and defect sites in the nanocarbon samples. The order of the surface functional groups affecting the ORR activity is as follows: carboxyl > carbonyl > hydroxyl groups. The electron transfer number of the nanocarbon samples synthesized from raw materials containing DO for the ORR were close to three at low potentials, which is larger than that of the nanocarbon sample synthesized from BZ100, indicating that the presence of the DO in the raw materials contributes to the improvement of the ORR activity. We believe that the solution plasma process can be an effective means of synthesizing nanocarbon materials containing hetero-atoms for highly functional metal-air batteries and fuel cell applications.

References

- 1 J. R. Miller and A. F. Burke, *Electrochem. Soc. Interface*, 2008, **17**, 53.
- 2 S. W. Lee, N. Yabuuchi, B. M. Gallant, S. Chen, B.-S. Kim, P. T. Hammond and Y. Shao-Horn, *Nat. Nanotechnol.*, 2010, **5**, 531.
- 3 J. M. Tarascon and M. Armand, *Nature*, 2001, **414**, 459.
- 4 A. Chen and P. Holt-Hindle, *Chem. Rev.*, 2010, **110**, 3767.
- 5 X. Ma, H. Meng, M. Cai and P. Shen, *J. Am. Chem. Soc.*, 2012, **134**, 1954.
- 6 G. Lota, K. Fic and E. Frackowiak, *Energy Environ. Sci.*, 2011, **4**, 1592.
- 7 P. Simon and A. F. Burke, *Electrochem. Soc. Interface*, 2008, **17**, 38.
- 8 P. Simon and Y. Gogotsi, *Nat. Mater.*, 2008, **7**, 845.
- 9 Y. Zhao, L. Yang, S. Chen, X. Wang, Y. Ma, Q. Wu, Y. Jiang, W. Qian and Z. Hu, *J. Am. Chem. Soc.*, 2013, **135**, 1201.
- 10 B. Winther-Jensen, O. Winther-Jensen, M. Forsyth and D. R. MacFarlane, *Science*, 2008, **321**, 671.
- 11 Y. Zheng, Y. Jiao, J. Chen, J. Liu, J. Liang, A. Du, W. Zhang, Z. Zhu, S. C. Smith, M. Jaroniec, G. Q. Lu and S. Z. Qiao, *J. Am. Chem. Soc.*, 2011, **133**, 20116.
- 12 D. Yu, E. Nagelli, F. Du and L. Dai, *J. Phys. Chem. Lett.*, 2010, **1**, 2165.
- 13 Z. Schniepp, Y. Zhang, M. J. Hollamby, B. R. Pauw, M. Tanaka, Y. Matsushita and Y. Sakka, *J. Mater. Chem. A*, 2013, **1**, 13576.
- 14 H. Wang, T. Maiyalagan and X. Wang, *ACS Catal.*, 2012, **2**, 781.
- 15 D. S. Geng, S. L. Yang, Y. Zhang, J. L. Yang, J. Liu, R. Y. Li, T. K. Sham, X. L. Sun, S. Y. Ye and S. Knights, *Appl. Surf. Sci.*, 2011, **257**, 9193.
- 16 F. M. Hassan, V. Chabot, J. Li, B. K. Kim, L. R. Sandoval and A. Yu, *J. Mater. Chem.*, 2013, **1**, 2904.
- 17 Y. Zhang, K. Fugane, T. Mori, L. Niu and J. Ye, *J. Mater. Chem.*, 2012, **22**, 6575.
- 18 L. Yang, S. Jiang, Y. Zhao, L. Zhu, S. Chen, X. Wang, Q. Wu, J. Ma, Y. Ma and Z. Hu, *Angew. Chem., Int. Ed.*, 2011, **50**, 7132.
- 19 K. Suggs, V. Person and X.-Q. Wang, *Nanoscale*, 2011, **3**, 2465.
- 20 S. W. Lee, B. M. Gallant, Y. Lee, N. Yoshida, D. Y. Kim, Y. Yamada, S. Noda, A. Yamada and Y. Shao-Horn, *Energy Environ. Sci.*, 2012, **5**, 5437.
- 21 H. R. Byon, S. W. Lee, S. Chen, P. T. Hammond and Y. Shao-Horn, *Carbon*, 2011, **49**, 457.
- 22 S. W. Lee, B. M. Gallant, H. R. Byon, P. T. Hammond and Y. Shao-Horn, *Energy Environ. Sci.*, 2011, **4**, 1972.
- 23 S. W. Lee, B.-S. Kim, S. Chen, Y. Shao-Horn and P. T. Hammond, *J. Am. Chem. Soc.*, 2009, **131**, 671.
- 24 D. G. Tong, P. Wu, P. K. Su, D. Q. Wang and H. Y. Tian, *Mater. Lett.*, 2012, **70**, 94.
- 25 X. Hu, S.-P. Cho, O. Takai and N. Saito, *Cryst. Growth Des.*, 2012, **12**, 119.
- 26 G. Panomsuwan, N. Zettsu and N. Saito, *Mater. Res. Soc. Symp. Proc.*, 2013, **1509**, cc09.
- 27 T. Shirafuji, Y. Himeno, N. Saito and O. Takai, *J. Photopolym. Sci. Technol.*, 2013, **26**, 507.
- 28 A. Watthanaphanit, G. Panomsuwan and N. Saito, *RSC Adv.*, 2014, **4**, 1622.
- 29 J. Kang, O. L. Li and N. Saito, *Carbon*, 2013, **60**, 292.
- 30 N. Sano, H. Wang, I. Alexandrou, M. Chowalla, K. B. K. Teo and G. A. Amaratunga, *J. Appl. Phys.*, 2002, **92**, 2783.
- 31 S. Scalese, V. Scuderi, S. Bagiante, F. Simone, P. Russo, L. D'Urso, G. Compagnini and V. Privitera, *J. Appl. Phys.*, 2010, **107**, 014304.
- 32 E. K. Athassiou, R. N. Grass and W. J. Stark, *Nanotechnology*, 2006, **17**, 1668.
- 33 T. Kizu, S. Aikawa, K. Takekoshi and E. Nishikawa, *e-Journal of Surface Science and Nanotechnology*, 2013, **11**, 8.
- 34 N. Andreeva, T. Ishizaki, P. Baroch and N. Saito, *Jpn. J. Appl. Phys.*, 2012, **51**, 126201.
- 35 Y. Hishiyama and M. Nakamura, *Carbon*, 1995, **33**, 1399.
- 36 Z. Q. Li, C. J. Lu, Z. P. Xia, Y. Zhou and Z. Luo, *Carbon*, 2007, **45**, 1686.
- 37 K. N. Kudin, B. Ozbas, H. C. Schniepp, R. K. Prud'homme, I. A. Aksay and R. Car, *Nano Lett.*, 2007, **8**, 36.

- 38 Z.-S. Wu, W. Ren, L. Gao, J. Zhao, Z. Chen, B. Liu, D. Tang, B. Yu, C. Jiang and H.-M. Cheng, *ACS Nano*, 2009, **3**, 411.
- 39 N. Soin, S. Sinha Roy, S. Roy, K. S. Hazra, D. S. Misra, T. H. Lim, C. J. Hetherington and J. A. McLaughlin, *J. Phys. Chem. C*, 2011, **115**, 5366.
- 40 L. G. Cancado, K. Takai, T. Enoki, M. Endo, Y. A. Kim, H. Mizusaki, A. Jorio, L. N. Coelho, R. Magalhaes-Paniago and M. A. Pimenta, *Appl. Phys. Lett.*, 2006, **88**, 163106.
- 41 H. Wang, T. Maiyalagan and X. Wang, *ACS Catal.*, 2012, **2**, 781.
- 42 S. Mikhailov, *Physics and Applications of Graphene-Experiments*, InTech Publisher, Croatia, 2011, ch. 5.
- 43 P. C. Wong, Y. S. Li and K. A. R. Mitchell, *Appl. Surf. Sci.*, 1995, **84**, 245.
- 44 R. W. Paynter, *Surf. Interface Anal.*, 1998, **26**, 674.
- 45 K. Tammeveski, K. Kontturi, R. J. Nichols, R. J. Potter and D. J. Schiffrin, *J. Electroanal. Chem.*, 2001, **515**, 101.
- 46 A. J. Bard and L. R. Faulkner, *Electrochemical Methods: Fundamentals and Application*, John Wiley & Sons, New York, 2nd edn, 2000, p. 335.
- 47 I. Roche, E. Chaînet, M. Chatenet and J. Vondrák, *J. Phys. Chem. C*, 2011, **111**, 1434.
- 48 I. Kruusenberg, J. Beis and M. Arulepp, *J. Solid State Electrochem.*, 2010, **14**, 1269.
- 49 S. Wang, D. Yu and L. Dai, *J. Am. Chem. Soc.*, 2011, **133**, 5182.
- 50 G. Jürmann, D. J. Schiffrin and K. Tammeveski, *Electrochim. Acta*, 2007, **53**, 390.
- 51 R. A. Sidik, A. B. Anderson and N. P. Subramanian, *J. Phys. Chem. B*, 2006, **110**, 1787.
- 52 E. Yeager, *Electrochim. Acta*, 1984, **29**, 1527.
- 53 Z. Shi, J. Zhang, Z. Liu, H. Wang and D. Wilkinson, *Electrochim. Acta*, 2006, **51**, 1905.
- 54 H. Kim, K. Lee, S. I. Woo and Y. Jung, *Phys. Chem. Chem. Phys.*, 2011, **13**, 17505.
- 55 K. Gong, F. Du, Z. Xia, M. Durstock and L. Dai, *Science*, 2009, **323**, 760.
- 56 R.-S. Zhong, Y.-H. Qin, D.-F. Niu, J.-W. Tian, X.-S. Zhang, X.-G. Zhou, S.-G. Sun and W.-K. Yuan, *J. Power Sources*, 2013, **225**, 192.